IEEE Access
Multidisciplinary | Rapid Review | Open Access Journal

Received 16 November 2023, accepted 5 December 2023, date of publication 12 December 2023,
date of current version 19 December 2023.

Digital Object Identifier 10.1109/ACCESS.2023.3341508

APPLIED RESEARCH

Reactive Power Controller for Single Phase Dual Active Bridge DC–DC Converters

HAMID NASEEM, (Student Member, IEEE), AND JUL-KI SEOK, (Senior Member, IEEE)
Department of Electrical Engineering, Yeungnam University, Gyeongsan, Gyeongbuk 38541, South Korea

Corresponding author: Jul-Ki Seok (doljk@ynu.ac.kr)

This work was supported by the 2020 Yeungnam University Research Grant.

ABSTRACT In this study, we have proposed a triple-phase shift power-level controller (TPSPC) that achieves zero reactive power generation by fundamental components in a single-phase dual active bridge (DAB) DC-DC converter. The proposed power controller efficiently controls the active and reactive powers independently. The TPSPC regulates the phase shifts between the two H-bridges and inner phase shifts within each bridge to effectively eliminate the reactive power of the fundamental components in the converter. This elimination significantly decreases the inductor current across all load conditions without requiring a multiple mode analysis for the different operational states or any overly complex control functions. Unlike dual-phase shift power-level controllers, the TPSPC uniquely manages each phase shift independently, reducing the inductor current and significantly enhancing the performance. The versatile TPSPC methodology demonstrated in this study is promising for various DAB applications, such as aerospace systems, hybrid electric vehicle charging systems, and the asynchronous interconnection of micro-grids.

INDEX TERMS Dual active bridge converter, power-level controller, triple-phase shift.

I. INTRODUCTION

The power flow in a dual active bridge (DAB) converter is primarily controlled by varying the phase difference between the voltages of the two H-bridges. The single-phase shift (SPS) modulation is a widely utilized control approach [1] in which the direction and magnitude of active power are managed by manipulating the phase difference between two H-bridges. However, this method can result in a high circulating current, primarily when the voltages on the primary and secondary sides are unequal. Several strategies [2], [3], [4], [5], [6], [7], [8] to overcome this drawback have been proposed in previous studies; inner phase shifts were added to the SPS method to minimize circulating current or reduce reactive power. Reactive power elimination was initially introduced in [9]; subsequently, a reactive power regulation technique based on a triple-phase shift was proposed in [10], [11], and [12] to minimize the circulating current. However, in these methods [2], [3], [4], [5], [6], [7], [8], [9], [10], [11], [12], the reactive power was not directly controlled to reduce the inductor current. Instead, these approaches involved meticulous phase-shift signal selection through predefined mode transitions, complex switching table schemes, and gain selections. To address the intricacies associated with mode switching, modulation schemes based on the frequency domain [13], [14], [15] have been introduced to minimize the reactive power. Efforts to minimize or eliminate the reactive power in DAB converters have led to several innovative methods. A variable inductance structure for DAB converters is introduced [16] to reduce reactive power by adjusting the inductor value and applying phase shift modulation. In [17], an artificial intelligence (AI) based scheme utilizing the advanced deep reinforcement learning algorithm minimizes the reactive power in DAB converters. The AI agent optimizes real-time control to achieve the low circulating power between the H-bridges. An unconventional approach in [18] employs a sinusoidal pulse width-phase shift modulation scheme with Lagrange's Multiplier Method to reduce reactive power and current stress in DAB converters. In [19], a proportional-value modulation technique is proposed for the bidirectional reactive current elimination in DAB converters. A frequency-modulated scheme is introduced [20], incorporating a variable-frequency control algorithm to linearize the nonlinear phase shift angle function to minimize the reactive

The associate editor coordinating the review of this manuscript and approving it for publication was Zhe Zhang.

power flow. However, these methods indirectly manage reactive power to minimize inductor current and do not eliminate reactive power completely.

A frequency-domain-based dual-phase shift power-level controller (DPSPC) [21] was presented, which offered the ability to directly and independently regulate the active and reactive powers. This approach significantly decreased the inductor current compared with the SPS and dual-phase shift [3] methods. However, the DPSPC relied on only two phase shifts as control variables, and the inner phase shift of the secondary H-bridge remained unaltered. This constraint curtailed the potential to optimize the maximum power flow and efficiency under light load conditions.

Therefore, in this study, we introduced a triple-phase shift power-level controller (TPSPC) that eliminates the reactive power of fundamental components irrespective of the connected load. The TPSPC accurately follows the specified power command to regulate the output voltage at each sampling point without requiring multi-mode analysis for different operational states or any overly complex control functions. Notably, the proposed TPSPC methodology significantly reduces the root mean square (rms) inductor current, thereby achieving reductions of up to 51% and 31% compared with the SPS and DPSPC modulation schemes, respectively.

II. MODELING OF SINGLE-PHASE DUAL ACTIVE BRIDGE CONVERTER

The schematic in Fig. 1 depicts the circuit configuration of a single-phase DAB converter. The active power flows from the primary to the secondary-side H-bridge inverter through a high-frequency transformer. The voltages of the primary and secondary windings of the transformer are denoted as $v_{pr}(t)$ and $v_{sr}(t)$, respectively. V_{in} and V_{out} represent the input and output voltages of the DAB converter, respectively. L_t and R_t represent the leakage inductance and parasitic resistance of the transformer windings, respectively. The fundamental components of the voltages of the primary and secondary sides, along with the phase shifts between the bridges during one switching cycle in the steady state, are shown in Fig. 2. The inner phase shifts of the two inverters are denoted as d_1 and d_2, respectively, and d_3 represents the phase shift between the voltages of the primary and secondary windings of the transformer. The power flow in the converter is regulated by varying the phase shift d_3 or amplitude of the fundamental component of the two H-bridge inverter voltages with d_1 and d_2, where $0 \leq d_1 \leq 1$, $0 \leq d_2 \leq 1$, and $-1 \leq d_3 \leq 1$.

The primary and secondary voltages across the transformer windings are mathematically expressed as [22]:

$$v_{pr}(t) = \sum_{n=1,3,5..}^{\infty} \frac{4V_{in}}{n\pi} \cos\left(n\pi \frac{d_1}{2}\right) \sin\left(n\omega_s t\right), \tag{1a}$$

$$v_{sr}(t) = \sum_{n=1,3,5..}^{\infty} \frac{4V_{out}}{n\pi} \cos\left(n\pi \frac{d_2}{2}\right) \sin\left(n\omega_s t - n\varphi\right), \tag{1b}$$

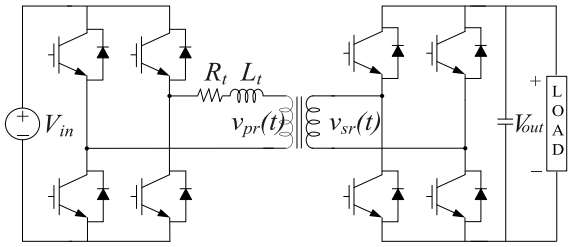

FIGURE 1. Dual active bridge converter.

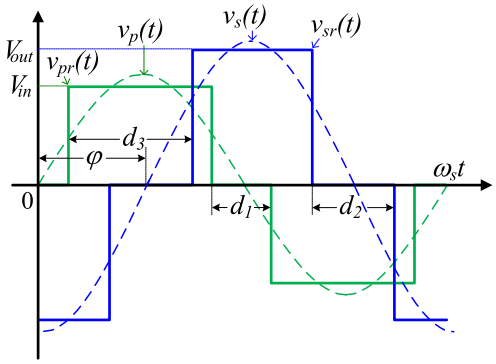

FIGURE 2. Fundamental component analysis.

$$\varphi = \left(d_3 + \frac{d_2 - d_1}{2}\right)\pi, \tag{1c}$$

where ω_s and φ represent the angular frequency and phase shift of individual fundamental components, respectively.

The AC equivalent circuit of the DAB converter considering only the fundamental components is illustrated in Fig. 3.

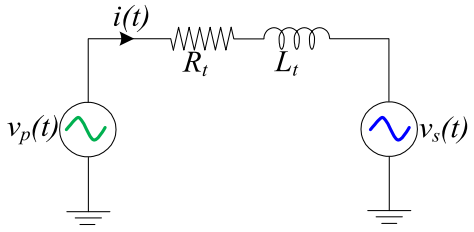

FIGURE 3. AC equivalent circuit diagram.

The fundamental component of current through the inductor is denoted as $i(t)$. Since both inverters operate at the same switching frequency, the inductor current and transformer's winding voltages can be seen as rotating vectors i, v_p, and v_s all rotating at the identical angular speed of ω_s. The vector diagram illustrating their relationship is depicted in Fig. 4.

The projection of voltages and current in the dq rotating reference frame are employed throughout the entire analysis and power controller design in this paper. The primary and secondary voltages $\boldsymbol{v}_{pdq}(t)$ and $\boldsymbol{v}_{sdq}(t)$ in the dq rotating ref-

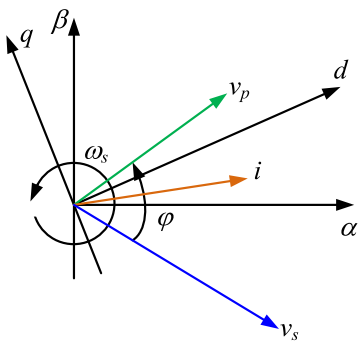

FIGURE 4. Vector Diagram.

erence frame can be given as:

$$\begin{bmatrix} v_{pd}(t) \\ v_{pq}(t) \end{bmatrix} = \frac{4v_{in}(t)}{\pi} \cos\left(\pi \frac{d_1}{2}\right) \begin{bmatrix} \sin \pi d_3 \\ \cos \pi d_3 \end{bmatrix}, \tag{2a}$$

$$\begin{bmatrix} v_{sd}(t) \\ v_{sq}(t) \end{bmatrix} = \frac{4v_{out}(t)}{\pi} \cos\left(\pi \frac{d_2}{2}\right) \begin{bmatrix} \sin\left(\pi \frac{d_2-d_1}{2}\right) \\ \cos\left(\pi \frac{d_2-d_1}{2}\right) \end{bmatrix}, \tag{2b}$$

where $v_{in}(t)$ and $v_{out}(t)$ represent the input voltage of the primary H-bridge inverter and the output voltage of the secondary H-bridge inverter, respectively.

The inductor current in the dq rotating reference frame $i_{Ld}(t)$ and $i_{Lq}(t)$ can be determined as:

$$\begin{bmatrix} i_{Ld}(t) \\ i_{Lq}(t) \end{bmatrix} = \frac{1}{\sqrt{R_t^2 + \omega_s^2 L_t^2}} \begin{bmatrix} v_{pq}(t) - v_{sq}(t) \\ v_{sd}(t) - v_{pd}(t) \end{bmatrix}. \tag{3}$$

III. TRIPLE-PHASE SHIFT POWER-LEVEL CONTROLLER DESIGN

A dq rotating reference frame is adopted in this study to analyze the converter's instantaneous power. We assumed an imaginary axis orthogonal to the real axis with the same angular frequency. The voltage equations in the dq rotating reference frame are mathematically expressed as follows:

$$\frac{di_{Ld}(t)}{dt} = \frac{1}{L_t} v_{pd}(t) - \frac{1}{L_t} v_{sd}(t) - \frac{R_t}{L_t} i_{Ld}(t) - \omega_s i_{Lq}(t). \tag{4a}$$

$$-\frac{di_{Lq}(t)}{dt} = \frac{1}{L_t} v_{pq}(t) - \frac{1}{L_t} v_{sq}(t) - \frac{R_t}{L_t} i_{Lq}(t) + \omega_s i_{Ld}(t). \tag{4b}$$

The instantaneous active and reactive powers supplied from the source through the fundamental components can be mathematically expressed as follows:

$$p(t) = \frac{1}{2}\left(v_{pd}(t) i_{Ld}(t) + v_{pq}(t) i_{Lq}(t)\right). \tag{5a}$$

$$q(t) = \frac{1}{2}\left(v_{pq}(t) i_{Ld}(t) - v_{pd}(t) i_{Lq}(t)\right). \tag{5b}$$

A unique voltage command was obtained in the dq rotating reference frame for each sampling time by combining (1), (4) and (5), as follows:

$$v_{pd}^*(k)$$

$$= 2\left(\frac{i_{Ld}(k)}{i_{Ld}^2(k) + i_{Lq}^2(k)}\right)\begin{pmatrix} p^*(k) + \frac{R_t T_s}{L_t} p(k) - \omega_s T_s q(k) \\ -\frac{T_s}{2L_t}\begin{pmatrix} v_{pd}^2(k) + v_{pq}^2(k) \\ -v_{pd}(k) v_{sd}(k) \\ -v_{pq}(k) v_{sq}(k) \end{pmatrix} \end{pmatrix} \tag{6a}$$

$$- 2\left(\frac{i_{Lq}(k)}{i_{Lq}^2(k) + i_{Ld}^2(k)}\right)\begin{pmatrix} q^*(k) + \frac{R_t T_s}{L_t} q(k) + \omega_s T_s p(k) \\ -\frac{T_s}{2L_t}\begin{pmatrix} v_{pd}(k) v_{sq}(k) \\ -v_{pq}(k) v_{sd}(k) \end{pmatrix} \end{pmatrix},$$

$$v_{pq}^*(k)$$

$$= 2\left(\frac{i_{Lq}(k)}{i_{Ld}^2(k) + i_{Lq}^2(k)}\right)\begin{pmatrix} p^*(k) + \frac{R_t T_s}{L_t} p(k) - \omega_s T_s q(k) \\ -\frac{T_s}{2L_t}\begin{pmatrix} v_{pd}^2(k) + v_{pq}^2(k) \\ -v_{pd}(k) v_{sd}(k) \\ -v_{pq}(k) v_{sq}(k) \end{pmatrix} \end{pmatrix} \tag{6b}$$

$$+ 2\left(\frac{i_{Ld}(k)}{i_{Lq}^2(k) + i_{Ld}^2(k)}\right)\begin{pmatrix} q^*(k) + \frac{R_t T_s}{L_t} q(k) + \omega_s T_s p(k) \\ -\frac{T_s}{2L_t}\begin{pmatrix} v_{pd}(k) v_{sq}(k) \\ -v_{pq}(k) v_{sd}(k) \end{pmatrix} \end{pmatrix},$$

where T_s and the superscript "$*$" represent the pulse-width modulation period and corresponding command variables, respectively.

The instantaneous phase angle θ of the fundamental component is mainly estimated by the arctangent function method or the synchronous frame method. The synchronous frame method is widely recognized in power electronics for better performance [23] and is chosen for angle estimation in this paper. The primary side voltage in $\boldsymbol{v}_{p\alpha\beta}$ in a stationary reference frame can be easily obtained from the Fourier series representation of voltage from (1) as:

$$v_{p\alpha}(t) = \frac{4V_{in}}{\pi} \cos\left(\pi \frac{d_1}{2}\right) \sin(\omega_s t + \delta). \tag{7a}$$

$$v_{p\beta}(t) = \frac{4V_{in}}{\pi} \cos\left(\pi \frac{d_1}{2}\right) \cos(\omega_s t + \delta). \tag{7b}$$

The angle δ signifies the phase shift between the voltages of the primary and secondary windings of the transformer. This phase shift can be achieved by either lagging the secondary side voltage or leading the primary side voltage. In this study, the primary side voltage is adjusted to lead, signifying that under typical operating conditions δ equals d_3.

Applying the Park transformation to the voltage signals $v_{p\alpha}$ and $v_{p\beta}$, the voltage components $\hat{v}_{pd}(t)$ and $\hat{v}_{pq}(t)$ in the dq rotating reference frame can be expressed as:

$$\begin{bmatrix} \hat{v}_{pd}(t) \\ \hat{v}_{pq}(t) \end{bmatrix} = \begin{bmatrix} \cos(\hat{\theta}) & \sin(\hat{\theta}) \\ -\sin(\hat{\theta}) & \cos(\hat{\theta}) \end{bmatrix} \begin{bmatrix} v_{p\alpha}(t) \\ v_{p\beta}(t) \end{bmatrix}, \tag{8}$$

where $\hat{\theta}$ is the estimated phase angle.

The value of v_{pd} can be computed using (2). The difference between v_{pd} and $\hat{v}_{pd}$ is employed within the control Proportional-Integral (PI) loop to extract the frequency and phase angle, as illustrated in Fig. 6. The estimated frequency can be obtained as:

$$\hat{\omega}_s(t) = K_p \cdot e(t) + K_i \int e(t)dt + \omega_s(t), \tag{9}$$

where $e(t) = v_{pd}(t) - \hat{v}_{pd}(t)$, and K_p and K_i are the gains of the PI controller.

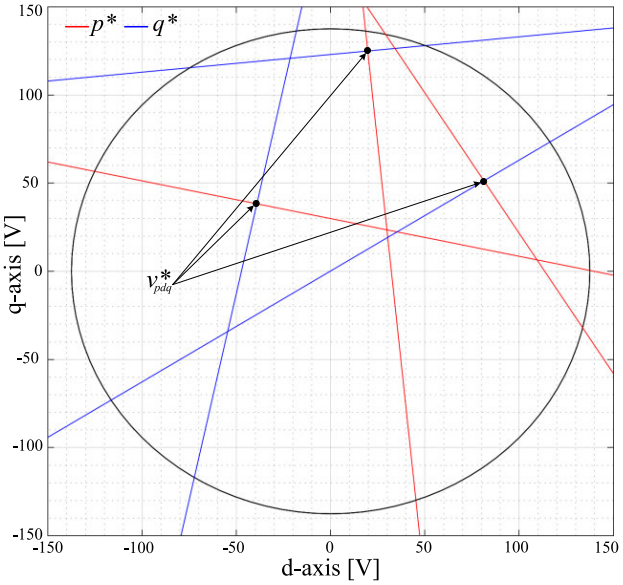

FIGURE 5. Voltage vector solutions for active and reactive power commands at three different sampling points in dq voltage plane.

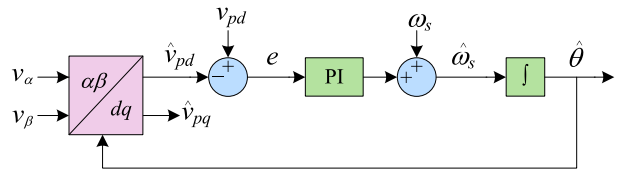

FIGURE 6. Synchronous frame-based angle estimation.

Subsequently, the estimated phase angle can be obtained as:

$$\hat{\theta}(t) = \int \hat{\omega}_s(t)dt + \hat{\omega}_s(0). \tag{10}$$

When the error denoted as '$e(t)$' converges to zero, the phase angle difference $\theta(t) - \hat{\theta}(t)$ will also approach zero. This implies that the actual angle and the estimated angle become identical.

Consequently, $\theta(t) = \hat{\theta}(t)$.

The imaginary stationary voltage is always orthogonal to the real axis voltage. Furthermore, the frequency of the fundamental component remains constant under usual operating circumstances and the gains can be easily calculated by ensuring system stability.

The graphical representation delineates the voltage commands at three distinct sampling points during the transient period is depicted in Fig. 5. These voltage commands are computed from the intersection of the active and reactive powers in the dq voltage plane. The circle defines the physical limit of the DC-link voltage of the converter. The overall control block diagram of the TPSPC is shown in Fig. 7.

A Proportional-Integral controller generates an active power command that regulates the output voltage to follow the reference voltage (V_{ref}). Meanwhile, the reactive power generator provides a reactive power command to minimize the inductor current.

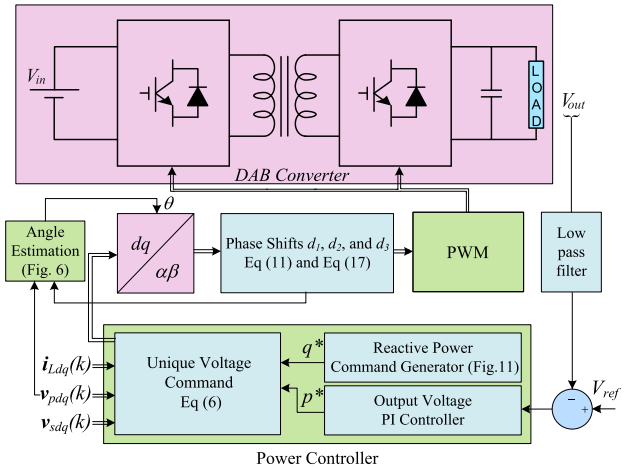

FIGURE 7. Overall control block diagram.

The voltage command $\boldsymbol{v}_{pdq}{}^*$ in (6) is converted into a stationary reference frame voltage vector with amplitude V_m and a phase shift ψ for the required active and reactive power commands.

Consequently, the phase shifts, d_1 and d_3, for the next sample are obtained as follows:

$$d_1\,(k+1) = \frac{2}{\pi}\cos^{-1}\left(\frac{\pi}{4}\cdot\frac{V_m}{V_{in}}\right), \tag{11a}$$

$$d_3\,(k+1) = \frac{\psi}{\pi}, \tag{11b}$$

where d_1 and d_3 are the manipulated inputs of the proposed controller, which effectively controls the active and reactive power independently. This approach eliminates the need for multiple modes of analysis for different operational states and overly complex control functions.

IV. REACTIVE POWER CONTROLLER

The total active power can be expressed as the sum of fundamental odd frequency components as [13]:

$$\begin{aligned} P_T &= \sum_{n=1,3,5..}^{\infty} P_n \\ &= \sum_{n=1,3,5..}^{\infty} \frac{8V_{in}V_{out}}{n^3\pi^2\omega_s L_t} \\ &\quad \left(\cos\left(n\pi\frac{d_1}{2}\right)\cos\left(n\pi\frac{d_2}{2}\right)\sin\left(n\varphi\right)\right). \end{aligned} \tag{12}$$

The curves to represent different active power components and the total active power are shown in Fig. 8. All active power components are normalized using $P_N = V_{in*}V_{out}/(8_*f_{s*}L_t)$, where f_s is the switching frequency.

It can be observed that the curve representing the total power achieved by the traditional piecewise linear method which attains a maximum value of 1. Additionally, among all components (P_1, P_3, and P_5), the fundamental component of active power (P_1) stands out with the highest amplitude, closely resembling the overall power obtained through the traditional piecewise linear method (P_T).

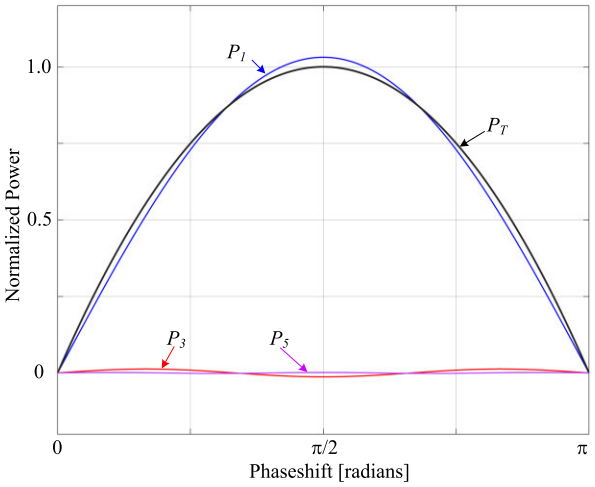

FIGURE 8. Active power curves of different frequencies component.

The details of the fundamental active and reactive powers are provided in [13]:

$$p(t) = \frac{v_1(t)\, v_2(t) \sin(\varphi)}{\omega_s L_t}, \tag{13a}$$

$$q(t) = \frac{v_1(t)\,(v_1(t) - v_2(t)\cos(\varphi))}{\omega_s L_t}, \tag{13b}$$

where $v_1(t) = \frac{4V_{in}}{\sqrt{2}\pi} \cos\left(\pi \frac{d_1}{2}\right)$ and $v_2(t) = \frac{4V_{out}}{\sqrt{2}\pi} \cos\left(\pi \frac{d_2}{2}\right)$.

The active and reactive components of the inductor current are expressed as follows [24]:

$$i_{L\,active}(t) = \frac{v_2(t)\sin(\varphi)}{\omega_s L_t}. \tag{14a}$$

$$i_{L\,reactive}(t) = \frac{v_1(t) - v_2(t)\cos(\varphi)}{\omega_s L_t}. \tag{14b}$$

The inductor rms current in discrete time can be obtained from (13) and (14) as:

$$i_L(k) = \frac{1}{\omega_s L_t} \sqrt[4]{\begin{pmatrix} v_2^4(k) + 4\omega_s L_t \cdot v_2^2(k) \cdot q(k) \\ -4\omega_s^2 L_t^2 \cdot p^2(k) \end{pmatrix}}. \tag{15}$$

From (15), the rms current of the inductor can be effectively controlled by appropriately manipulating $v_2(k)$ and $q(k)$ under varying active power requirements. The condition for the minimum value of the inductor current is obtained by taking the partial derivative of (15) with respect to $v_2(k)$ and $q(k)$:

$$q(k) = 0 \;\text{ and }\; v_2(k) = \sqrt{2\omega_s L_t \cdot p(k)}. \tag{16}$$

Consequently, the inner phase shift d_2 is obtained from (16) as follows:

$$d_2(k) = \frac{2}{\pi} \cos^{-1}\left(\sqrt{\frac{\omega_s L_t \cdot p(k)}{4V_{out}^2}}\right). \tag{17}$$

However, in the DPSPC scheme, the inner phase shift of the secondary H-bridge d_2 remained fixed across all load conditions, limiting its potential to achieve higher power flow and efficiency. Conversely, the proposed TPSPC method actively adjusts d_2 based on the active power requirements, as shown in Fig. 9.

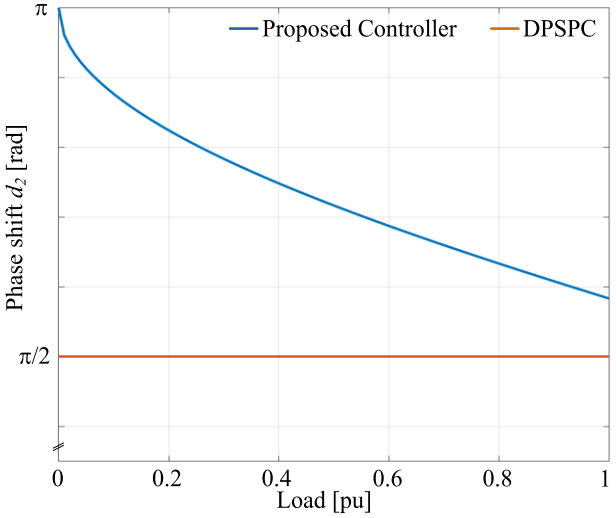

FIGURE 9. Inner phase shift d_2 over all load conditions.

The reactive power curves for different load conditions are shown in Fig. 10. The symbol '•' denotes instances of zero reactive power at a particular active power demand. The red vertical dashed lines denote the physical constraints on the primary H-bridge voltage. When the voltage required to achieve zero reactive power exceeds the physical limit, the reactive power command is obtained from (13) and (16) as follows:

$$q(k) = \frac{v^2(k)}{\omega_s L_t} - \sqrt{\frac{2v^2(k) \cdot p(k)}{\omega_s L_t} - p^2(k)}, \tag{18}$$

where $v(k)$ is defined as:

$$v(k) = \frac{1}{2}\sqrt{1 + 4\omega_s^2 L_t^2 \cdot p^2(k)}, \left(0 \le v(k) \le \frac{4V_{in}}{\sqrt{2}\pi}\right). \tag{19}$$

The necessary maximum leakage inductance (L_{max}) to achieve a zero reactive power of the fundamental components at a given rated power (P_{rated}) can be obtained as follows:

$$L_{max} = \frac{v^2}{\omega_s \cdot P_{rated}}, \quad \text{where } v = \frac{4V_{in}}{\sqrt{2}\pi}. \tag{20}$$

The reactive power command is obtained by utilizing (18) and (19), as shown in Fig. 11. Suppose the active power

demand is within the physical limit of the primary-side voltage, then (18) results in a reactive power command of zero. On the contrary, suppose the active power demand exceeds the physical limit of the input voltage; then, the same equation results in a reactive power command based on the input voltage of the converter.

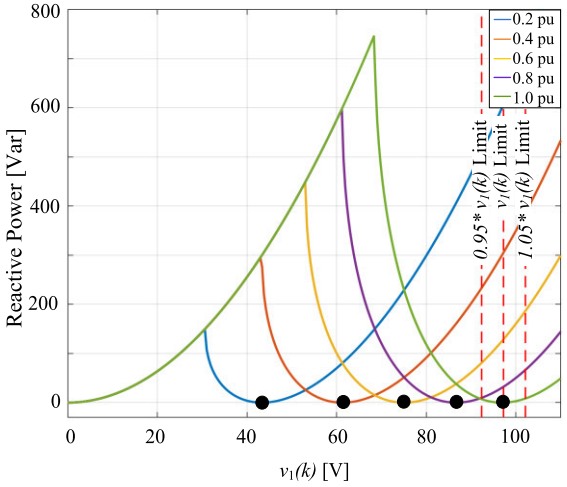

FIGURE 10. Reactive power curves with loads.

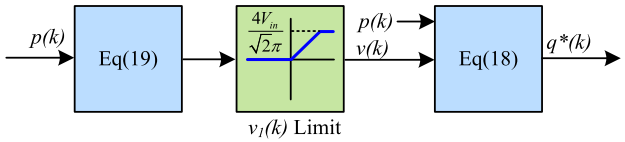

FIGURE 11. Block diagram to generate the reactive power command.

V. LOSS ESTIMATION

The main power losses in a DAB converter can be classified as switching and conduction losses.

A. SWITCHING LOSS CALCULATIONS

The switching losses in semiconductor devices are due to continuous switching (ON and OFF) transitions during which a device is simultaneously exposed to high voltage and current. The switching losses (P_{SW_on} and P_{SW_off}) in MOSFETs can be determined by:

$$P_{SW\_on} = \frac{1}{2} V_{DS} \cdot I_{DS} \cdot T_{ON} \cdot f_s, \tag{21a}$$

$$P_{SW\_off} = \frac{1}{2} V_{DS} \cdot I_{DS} \cdot T_{OFF} \cdot f_s, \tag{21b}$$

where V_{DS} and I_{DS} denote the voltage and current at the instant of switching, f_s represents switching frequency, and T_{ON} and T_{OFF} signify the time intervals during the ON and OFF switching events, respectively. It computes the power loss in a single switch during the turn ON and turn OFF switching transition. The cumulative losses for one H-bridge can be determined by multiplying it by 4.

B. CONDUCTION LOSS CALCULATIONS

Conduction losses are determined by the root mean square (rms) current (I_{Sp} rms and I_{Ss} rms) flowing through the primary and secondary inverters' switches. The rms switch current for primary and secondary side H-bridge inverters can be derived from the inductor's rms current (i_L) as [25]:

$$Is_p = \frac{i_L}{\sqrt{2}} \text{ and } Is_s = n \cdot \frac{i_L}{\sqrt{2}}, \tag{22}$$

where n is the transformer turn ratio.

Usually, high-frequency skin and proximity effects are ignored for power semiconductor devices. Consequently, the switch resistance for the chosen MOSFET(G3R75MT12D) is taken from datasheet values, where $R_{DS(on)}$ is specified as 75 mΩ. Since there are 4 switches in each H-bridge inverter, the conduction losses can be calculated as follows:

$$P_{P,cond} = 4R_{DS(on)} \cdot \left(Is_p\right)^2, \tag{23a}$$

$$P_{S,cond} = 4R_{DS(on)} \cdot \left(Is_s\right)^2, \tag{23b}$$

where $P_{P,cond}$ and $P_{S,cond}$ are the conduction losses of the primary and secondary side H-bridge inverters.

The analysis above clearly indicates that conduction and switching losses exhibit a direct proportionality to the inductor rms current. A reduction in inductor current leads to decreased losses, subsequently contributing to an improvement in overall efficiency.

VI. TEST RESULTS

The leakage inductance was selected from (20) for a 1.5 kW DAB converter, and the performances of the proposed law, SPS, and DPSPC modulation methods were tested on the converter with identical parameters.

A. SIMULATION RESULTS

The DAB converter parameters were computed to satisfy the requirements of an electric vehicle (EV) charging station. Notably, the charging voltage varies for different levels of EV charging systems [26], [27]. The charging voltage at a Level-1 charging station ranges between 200-400 V, whereas the mean value of the rectified voltage from a 120 V AC input is approximately 108 V.

The proposed power-level controller was validated using the Matlab Simulink 2022b software. The main parameters of the 1.5 kW EV charging system are as follows: $R_t = 50$ mΩ, $L_t = 33.3$ μH, switching frequency $f_s = 30$ kHz, transformer turn ratio = 1:1, input voltage $V_{in} = 108$ V, and output voltage $V_{out} = 250$ V.

To comprehensively analyze the effect of the TPSPC method, a test is performed at 0.6pu load for comparison with the SPS and DPSPC methods; the results are shown in Fig. 12. The obtained waveforms revealed that the inductor current and reactive power for the proposed method are the lowest among the three techniques, despite having an exact active power requirement. The results demonstrate the effectiveness of the TPSPC in minimizing inductor rms current and reactive

power, thus enhancing the overall performance of the converter.

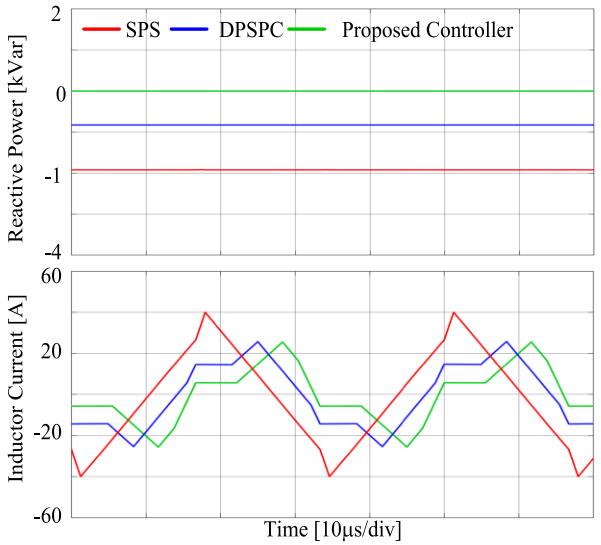

FIGURE 12. Inductor current and reactive power at 0.6pu load.

The time domain profiles of V_{out}, p^*, p, q^*, q, $\boldsymbol{v}_{pdq}{}^*$, and $\boldsymbol{v}_{pdq}$ arranged sequentially from top to bottom are shown in Fig. 13. At first, the converter operated at 0.2pu of the rated load at an output voltage of 250V. At t=50 ms, the connected load increased to full capacity. The TPSPC efficiently maintained the output voltage while concurrently regulating the active and reactive powers.

The inductor rms current across different load conditions is shown in Fig. 14. Notably, reductions of up to 51% and 31% were observed in comparison with the conventional SPS and DPSPC control methods, respectively. Efficiency calculations were performed for various loads to assess the efficacy of the TPSPC modulation scheme, as examined in [28]. As shown in Fig. 15, the TPSPC method outperformed the SPS and DPSPC methods, achieving a better performance.

B. EXPERIMENTAL RESULTS

A scaled-down laboratory prototype of the DAB converter was built by utilizing TMS320F28335 as the primary controller to demonstrate the effectiveness of the proposed control approach. The experimental setup, including the prototype DAB converter, DC power supplies, DC electronic load, differential probes, a sensor module, and a control board, is shown in Fig. 16.

The prototype input and output voltages were 108 V and 250 V, respectively. To minimize the switching losses, a silicon carbide MOSFET (G3R75MT12D) was utilized for the power switches, and the dead time between the switches was fixed at 150 ns for modulation. The inductor size was calculated using (20) at a rated power of 350 W.

Table 1 lists the primary electrical parameters of the experimental setup.

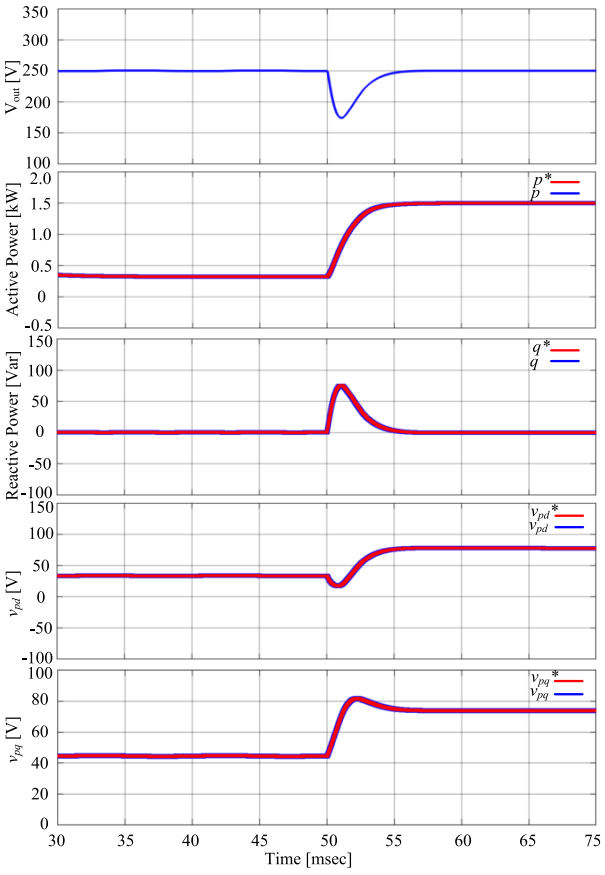

FIGURE 13. Results of the TPSPC at 0.2pu and full load.

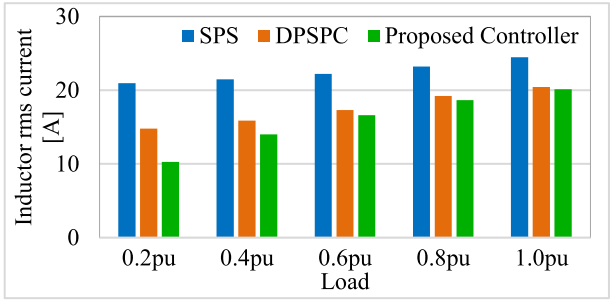

FIGURE 14. Inductor rms current at different loads.

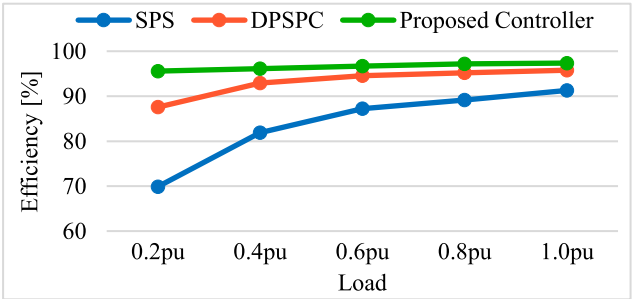

FIGURE 15. Efficiency curves at different loads.

Conventional voltage closed-loop control-based SPS and DPSPC controls were chosen for the comparative experiments to demonstrate the effectiveness of the proposed

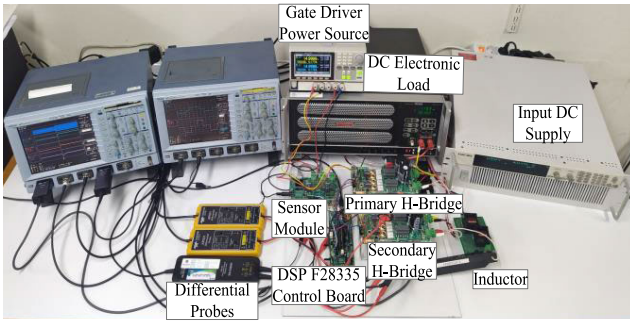

FIGURE 16. Experimental Setup.

TABLE 1. Electrical parameters of the experiment platform.

Electrical Parameters	Value	Unit
Rated Power	350	W
Input/Output Voltage V_{in}/V_{out}	108/250	V
Switching Frequency f_s	30	kHz
Inductance L_t	130	µH
Capacitance	235	µF
Dead Time	150	ns

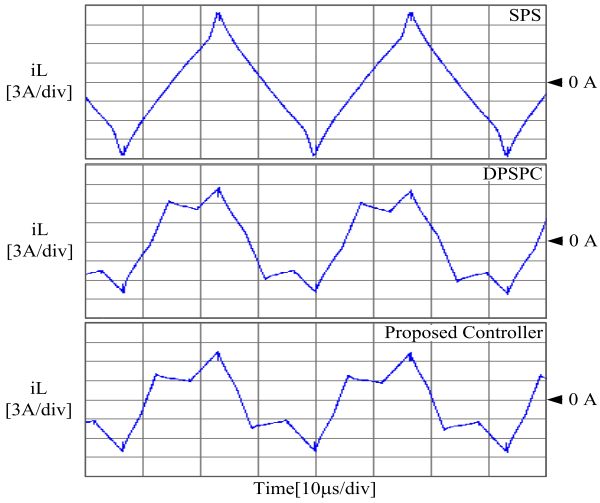

FIGURE 17. Inductor current at 0.6pu load.

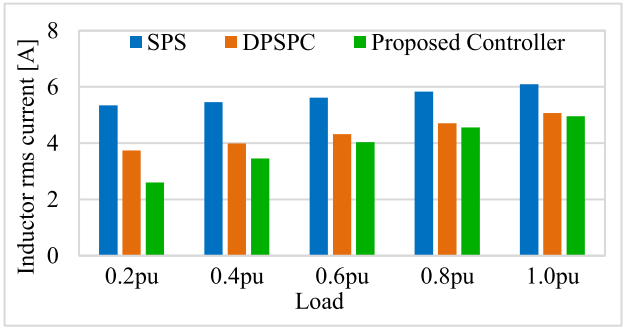

FIGURE 18. Inductor rms current at different loads.

approach more intuitively. The experimental waveform of the inductor current at a steady state for SPS, DPS, and the proposed approach at 0.6pu of the load is illustrated in Fig.17. The current through the inductor was lower at different load

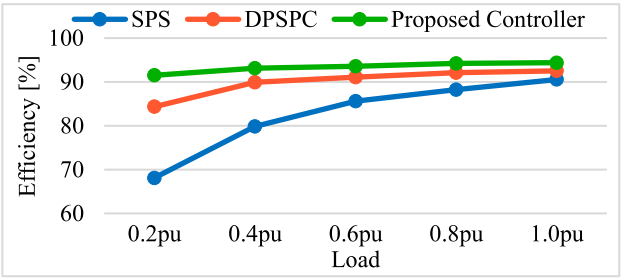

FIGURE 19. Efficiency curves at different loads.

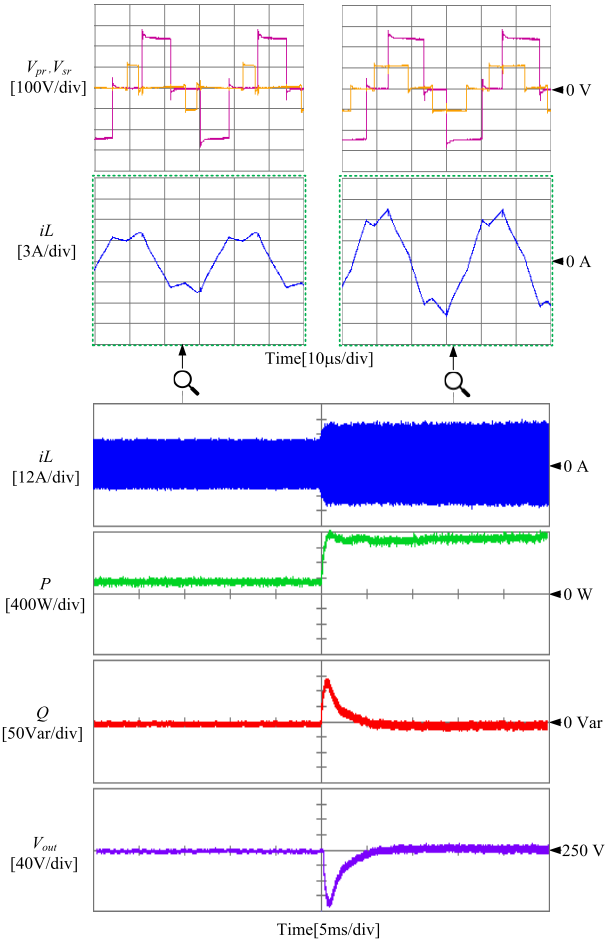

FIGURE 20. Control performance of the proposed controller.

levels compared with that of the SPS and DPSPC modulation methods, as shown in Fig. 18. To determine the power losses (P_d) at different operating conditions, the Digital DC Power Supply (Xantrex XDC 300-20) is used to obtain the input voltage and current, facilitating the calculation of input power (P_{in}). The output power (P_{out}) is determined by measuring the output voltage using a differential probe (Teledyne Lecroy HVD3102) with a digital oscilloscope (Lecroy LT374M). The load resistance value is obtained from the DC electronics load (Sorensen SLH-300-12-1200). The losses are subsequently computed using $P_d = P_{in} - P_{out}$, and the efficiency

is calculated accordingly. The measurement results closely align with the estimated values. The efficiency under various load conditions is illustrated in Fig. 19. The TPSPC method outperforms both SPS and DPSPC methods which demonstrates a better performance.

The control performance of the proposed method on the output voltage regulation for load variation from 0.2pu to full load is shown in Fig. 20. On the top, the waveforms of the primary and secondary side transformer winding voltage are displayed along with the zoomed-in waveforms of the inductor current at 0.2pu and 1.0pu loads.

Initially, the converter supplied a load of 70 W at 250 V from a 108 V source. Subsequently, the load suddenly changed to 350 W, whereas the input voltage remained unchanged. The fundamental active and reactive power signals shown in the figure were obtained using the two digital-to-analog channels of the control board. The proposed controller regulated the fundamental active and reactive powers while maintaining the output voltage and minimized the inductor current with a change in the load condition.

VII. CONCLUSION

This study introduced a triple-phase shift power-level controller that could independently control active and reactive powers in single-phase dual active bridge DC-DC converters. The proposed controller was developed by employing the fundamental components of current and voltages of the converter in a dq rotating reference frame. Phase shifts d_1 and d_3 were calculated from the voltage command vector, which was determined by calculating the intersection of the active and reactive powers in the dq voltage plane. To achieve zero reactive power across all load conditions, an empirical formula was presented to calculate the necessary maximum leakage inductance. The phase shift d_2 was actively manipulated to ensure zero reactive power according to the active power demand. The proposed controller provided control partitioning for active and reactive powers in the converter and achieved better efficiency and a lower inductor current across all load conditions.

REFERENCES

[1] S. Inoue and H. Akagi, "A bidirectional DC–DC converter for an energy storage system with galvanic isolation," *IEEE Trans. Power Electron.*, vol. 22, no. 6, pp. 2299–2306, Nov. 2007, doi: 10.1109/TPEL.2007.909248.

[2] B. Zhao, Q. Yu, and W. Sun, "Extended-phase-shift control of isolated bidirectional DC–DC converter for power distribution in microgrid," *IEEE Trans. Power Electron.*, vol. 27, no. 11, pp. 4667–4680, Nov. 2012, doi: 10.1109/TPEL.2011.2180928.

[3] H. Bai, Z. Nie, and C. C. Mi, "Experimental comparison of traditional phase-shift, dual-phase-shift, and model-based control of isolated bidirectional DC–DC converters," *IEEE Trans. Power Electron.*, vol. 25, no. 6, pp. 1444–1449, Jun. 2010, doi: 10.1109/TPEL.2009.2039648.

[4] W. Choi, K.-M. Rho, and B.-H. Cho, "Fundamental duty modulation of dual-active-bridge converter for wide-range operation," *IEEE Trans. Power Electron.*, vol. 31, no. 6, pp. 4048–4064, Jun. 2016, doi: 10.1109/TPEL.2015.2474135.

[5] J. Sun, L. Qiu, X. Liu, J. Zhang, J. Ma, and Y. Fang, "Optimal simultaneous PWM control for three-phase dual-active-bridge converters to minimize current stress in the whole load range," *IEEE J. Emerg. Sel. Topics Power Electron.*, vol. 9, no. 5, pp. 5822–5837, Oct. 2021, doi: 10.1109/JESTPE.2020.3047400.

[6] A. Tong, L. Hang, G. Li, X. Jiang, and S. Gao, "Modeling and analysis of a dual-active-bridge-isolated bidirectional DC/DC converter to minimize RMS current with whole operating range," *IEEE Trans. Power Electron.*, vol. 33, no. 6, pp. 5302–5316, Jun. 2018, doi: 10.1109/TPEL.2017.2692276.

[7] N. Hou, W. Song, and M. Wu, "Minimum-current-stress scheme of dual active bridge DC–DC converter with unified phase-shift control," *IEEE Trans. Power Electron.*, vol. 31, no. 12, pp. 8552–8561, Dec. 2016, doi: 10.1109/TPEL.2016.2521410.

[8] J. Huang, Y. Wang, Z. Li, and W. Lei, "Unified triple-phase-shift control to minimize current stress and achieve full soft-switching of isolated bidirectional DC–DC converter," *IEEE Trans. Ind. Electron.*, vol. 63, no. 7, pp. 4169–4179, Jul. 2016, doi: 10.1109/TIE.2016.2543182.

[9] H. Bai and C. Mi, "Eliminate reactive power and increase system efficiency of isolated bidirectional dual-active-bridge DC–DC converters using novel dual-phase-shift control," *IEEE Trans. Power Electron.*, vol. 23, no. 6, pp. 2905–2914, Nov. 2008, doi: 10.1109/TPEL.2008.2005103.

[10] S. Shao, M. Jiang, W. Ye, Y. Li, J. Zhang, and K. Sheng, "Optimal phase-shift control to minimize reactive power for a dual active bridge DC–DC converter," *IEEE Trans. Power Electron.*, vol. 34, no. 10, pp. 10193–10205, Oct. 2019, doi: 10.1109/TPEL.2018.2890292.

[11] S. Wang, Z. Zheng, C. Li, K. Wang, and Y. Li, "Time domain analysis of reactive components and optimal modulation for isolated dual active bridge DC/DC converters," *IEEE Trans. Power Electron.*, vol. 34, no. 8, pp. 7143–7146, Aug. 2019, doi: 10.1109/TPEL.2019.2897007.

[12] Y. A. Harrye, K. H. Ahmed, and A. A. Aboushady, "Reactive power minimization of dual active bridge DC/DC converter with triple phase shift control using neural network," in *Proc. Int. Conf. Renew. Energy Res. Appl. (ICRERA)*, Milwaukee, WI, USA, Oct. 2014, pp. 566–571, doi: 10.1109/ICRERA.2014.7016448.

[13] B. Zhao, Q. Song, W. Liu, G. Liu, and Y. Zhao, "Universal high-frequency-link characterization and practical fundamental-optimal strategy for dual-active-bridge DC–DC converter under PWM plus phase-shift control," *IEEE Trans. Power Electron.*, vol. 30, no. 12, pp. 6488–6494, Dec. 2015, doi: 10.1109/TPEL.2015.2430934.

[14] H. Shi, H. Wen, J. Chen, Y. Hu, L. Jiang, and G. Chen, "Minimum-reactive-power scheme of dual-active-bridge DC–DC converter with three-level modulated phase-shift control," *IEEE Trans. Ind. Appl.*, vol. 53, no. 6, pp. 5573–5586, Nov. 2017, doi: 10.1109/TIA.2017.2729417.

[15] T. Liu, X. Yang, W. Chen, Y. Li, Y. Xuan, L. Huang, and X. Hao, "Design and implementation of high efficiency control scheme of dual active bridge based 10 kV/1 MW solid state transformer for PV application," *IEEE Trans. Power Electron.*, vol. 34, no. 5, pp. 4223–4238, May 2019, doi: 10.1109/TPEL.2018.2864657.

[16] H. Xie, Y. Zhang, and F. Cai, "Variable inductance control of DAB converter to reduce reactive power," in *Proc. IEEE 6th Int. Electr. Energy Conf. (CIEEC)*, Hefei, China, May 2023, pp. 1360–1364, doi: 10.1109/CIEEC58067.2023.10166188.

[17] Y. Tang, W. Hu, D. Cao, N. Hou, Y. Li, Z. Chen, and F. Blaabjerg, "Artificial intelligence-aided minimum reactive power control for the DAB converter based on harmonic analysis method," *IEEE Trans. Power Electron.*, vol. 36, no. 9, pp. 9704–9710, Sep. 2021, doi: 10.1109/TPEL.2021.3059750.

[18] S. Chauhan and N. R. Tummuru, "An improvised modulation and control approach for dual active bridge DC–DC converter system," *IEEE Trans. Ind. Electron.*, pp. 1–11, 2023, doi: 10.1109/TIE.2023.3273248.

[19] A. Velazquez-Ibañez, J. R. Rodriguez, M. R. A. Paternina, and G. Carmona, "Elimination of circulating currents in PV-powered charging stations through dual active bridge modulation," in *Proc. North Amer. Power Symp. (NAPS)*, Salt Lake City, UT, USA, Oct. 2022, pp. 1–6, doi: 10.1109/NAPS56150.2022.10012157.

[20] O. Kwon, K.-S. Kim, and B.-H. Kwon, "Highly efficient single-stage DAB microinverter using a novel modulation strategy to minimize reactive power," *IEEE J. Emerg. Sel. Topics Power Electron.*, vol. 10, no. 1, pp. 544–552, Feb. 2022, doi: 10.1109/JESTPE.2021.3090097.

[21] H. Naseem and J.-K. Seok, "Reactive power control to minimize inductor current for single phase dual active bridge DC/DC converters," in *Proc. IEEE Energy Convers. Congr. Expo. (ECCE)*, Vancouver, BC, Canada, Oct. 2021, pp. 3261–3266, doi: 10.1109/ECCE47101.2021.9595553.
[22] A. Palamides and A. Veloni, "Fourier series," in *Signals and Systems Laboratory With MATLAB*, 1st ed. Boca Raton, FL, USA: CRC Press, 2011, ch. 5, pp. 249–279.
[23] B.-Y. Ren, Y.-R. Zhong, X.-D. Sun, and X.-Q. Tong, "A digital PLL control method based on the FIR filter for a grid-connected single-phase power conversion system," in *Proc. IEEE Int. Conf. Ind. Technol.*, Chengdu, China, Apr. 2008, pp. 1–6, doi: 10.1109/ICIT.2008.4608622.
[24] H. Naseem and J. K. Seok, "Triple-phase shift power-level controller (TPSPC) for single-phase dual active bridge (DAB) DC/DC converter," in *Proc. IEEE Energy Convers. Congr. Expo. (ECCE)*, Detroit, MI, USA, Oct. 2022, pp. 1–5, doi: 10.1109/ECCE50734.2022.9947623.
[25] F. Krismer and J. W. Kolar, "Accurate power loss model derivation of a high-current dual active bridge converter for an automotive application," *IEEE Trans. Ind. Electron.*, vol. 57, no. 3, pp. 881–891, Mar. 2010, doi: 10.1109/TIE.2009.2025284.
[26] S. Habib, M. M. Khan, F. Abbas, L. Sang, M. U. Shahid, and H. Tang, "A comprehensive study of implemented international standards, technical challenges, impacts and prospects for electric vehicles," *IEEE Access*, vol. 6, pp. 13866–13890, 2018, doi: 10.1109/ACCESS.2018.2812303.
[27] R. Collin, Y. Miao, A. Yokochi, P. Enjeti, and A. von Jouanne, "Advanced electric vehicle fast-charging technologies," *Energies*, vol. 12, no. 10, p. 1839, May 2019, doi: 10.3390/en12101839.
[28] O. M. Hebala, A. A. Aboushady, K. H. Ahmed, and I. Abdelsalam, "Generic closed-loop controller for power regulation in dual active bridge DC–DC converter with current stress minimization," *IEEE Trans. Ind. Electron.*, vol. 66, no. 6, pp. 4468–4478, Jun. 2019, doi: 10.1109/TIE.2018.2860535.

HAMID NASEEM (Student Member, IEEE) received the B.E. and M.Tech. degrees in electrical engineering from Aligarh Muslim University, India, in 2008 and 2012, respectively. He is currently pursuing the Ph.D. degree in electrical engineering with Yeungnam University, Gyeongsan, South Korea.

His research interests include high-power dc–dc conversion systems and power converters for automotive applications.

JUL-KI SEOK (Senior Member, IEEE) received the B.S., M.S., and Ph.D. degrees in electrical engineering from Seoul National University, Seoul, South Korea, in 1992, 1994, and 1998, respectively.

From 1998 to 2001, he was a Senior Engineer with the Production Engineering Center, Samsung Electronics, Suwon, South Korea. Since 2001, he has been a member of the School of Electrical Engineering, Yeungnam University, Gyeongsan, South Korea, where he is currently a Professor. His research interests include motor drives and power converter control.